Optical characterization of the impact of 100 keV protons on the optical properties of ZrO2 films prepared by ALD on fused silica substrates

Impact of proton irradiation on photoluminescent properties of C-doped ZrO_2 films prepared by ALD

Anna Sytchkova[a,*], Maria Lucia Protopapa[b], Emiliano Burresi[b], Paolo Olivero[c], Toni Dunatov[d], Zdravko Siketić[d], Leander Tapfer[b], Zhihao Wang[e,f], Hongbo He[e,g], Yanzhi Wang[e]

[a] Optical Coatings Group, Department for Energy Technologies and Renewable Sources, ENEA C.R. Casaccia, via Anguillarese 301, Rome 00123, Italy
[b] Department for Sustainability, ENEA C.R. Brindisi, SS 7 Appia Km 706, 72100 Brindisi, Italy
[c] Physics Department and "NIS" inter-departmental centre, University of Torino, via P. Giuria 1, 10125 Torino, Italy
[d] Laboratory for ion beam interaction, Institut Ruđer Bošković, Bijenička cesta 54, 10000 Zagreb, Croatia
[e] Laboratory of Thin Film Optics, Shanghai Institute of Optics and Fine Mechanics, No. 390 Qinghe Road, Jiading District, Shanghai 201800, China
[f] Center of Materials Science and Optoelectronics Engineering, University of Chinese Academy of Sciences, Beijing 100049, China
[g] Key Laboratory of Materials for High Power Laser, Shanghai Institute of Optics and Fine Mechanics, No. 390 Qinghe Road, Jiading District, Shanghai 201800, China

ARTICLE INFO

Keywords:
Optical coatings
Space radiation
Photoluminescence
Oxide

ABSTRACT

Amorphous C-doped zirconia thin films grown by ALD technique on fused silica substrates have high transmittance and significant photoluminescence (PL) capacity suitable for application as transparent material to convert high energy into lower energy photons as well as optical sensor of radiation. Due to carbon doping, zirconia films present three main PL transitions: Transition I and II at λ_{em}=450 nm (λ_{exc} =200 and 270 nm), related to sp^3 and sp^2 C-C bonds, and Transition II at λ_{em}=450 nm (λ_{exc}=300 nm) that can be assigned to C=O bonds which introduce n levels in the π- π* gap. Protons with energy of 100 keV and two values of fluences ($1\cdot10^{12}$ p+/cm^2 and $5\cdot10^{14}$ p+/cm^2) were used to modify the film properties. The changes induced by the radiation on the chemical composition of the films have been monitored as a function of irradiation dose using in-depth resolved XPS analysis. We demonstrate that C-Zr bonds are cleaved by protonation in favor of Zr-O, C-H and C=O bonds establishment. As a consequence, more defects levels are formed in the π- π* gap of carbon. Consequently, the emission due to Transitions I becomes more intense for high energy doses, getting intensity values close to Transitions I/II.

1. Introduction

Zirconium oxide (or zirconia, ZrO2) manufactured using atomic layer deposition (ALD) technique is a relatively new thin film material for optical applications. ALD enables conformal coating of complicated surfaces and allows for atomic-scale engineering of materials and therefore, for engineering of the optical properties of coatings.[1]

For many applications zirconia may be implemented in form of coatings, which may be a single film or a multilayer. Zirconia-based coatings are widely used for electric insulation in semiconductor devices [2], as thermal barriers [3]. Zirconia thin films represent also is a way to nanosize the material what may result an advantageous strategy in many demanding applications where traditionally bulky or powder materials have been used. The optical properties of thin films are known to be conditioned by their structure and microstructure, both dependent on the manufacturing method and the deposition conditions. Common ways to manufacture thin films of zirconia are (magnetron) sputtering [4] and electron-beam evaporation [5], although pulsed laser deposition [6] and sol-gel technique [7] may also be implemented. When starting from a metallic target, zirconia may be obtained by either thermal post-deposition annealing of sputtered zirconium, or by adding oxygen in the working gas during the deposition (reactive sputtering). Any of the aforementioned deposition techniques can provide polycrystalline or amorphous zirconia films of various packing densities and optical properties. In [8] ultrathin (about 3 nm thick) zirconia films prepared by Atomic Layer Deposition (ALD) were studied as a novel high-k material for use in microelectronics. The films were investigated for stoichiometry and surface roughness with the main focus on their electrical characteristics.

Zirconia remarkable catalytic properties [9] and chemical persistence are exploited in bio- and medical applications [10], and it is a promising solid electrolyte [11]. The particular combination of chemical, mechanical and optical properties characterizing this ceramics renders it quite unique for applications in particularly demanding fields like technologies for space and for nuclear energy [12]. For zirconium alloys used in corrosive and nuclear environments, zirconia is a protecting layer as it is exceptionally tolerant to radiation damage [13]. It enables radiation dosimeters and devices for radiation imaging [14].

Among properties of zirconia readily exploitable in optics are its high refractive index and significant luminescent yield [15]. Zirconia has three crystalline phases and both crystalline and amorphous zirconia coatings may be exploited. Stabilization and tuning of structural and hence mechanical and optical properties of zirconia is often used by doping with metals like Ce [16] and Er [17], or other ceramics like Y2O3 [18], CeO2 [19], Fe2O3 and MnO2 [20]. In particular, doping may be used to tune luminescence properties of zirconia.[21, 22]

Here we present a study on a set of C-doped amorphous thin films of zirconia manufactured by ALD for space applications. The films were prepared on fused silica substrates with a thickness of about 200 nm relevant for many optical devices. Our recent study [23] reported characterization of these films in terms of their complex refractive index and its in-depth variation prior and after the irradiation with 100 keV protons.

This article reports on the composition and the photo-induced luminescence (PL) ability of C-doped a-ZrO2 films. The origins of PL in zirconia is still a subject of discussion [24-26]. Oxygen vacancies [27] as well as impurities either deposition-dependent or absorbed upon exposure of the film to the environment [28, 29] are normally indicated as PL origins. It is also known that PL of zirconia is affected by both temperature regime and energetic particle irradiation [25]. In this study we show that the pivotal mechanism of the PL in our C-doped a-ZrO_2 films is the interaction of the carbon impurities with the protons and with over-stoichiometric oxygen induced by low-energy protons. Modification the PL of the films may find applications in dosimetry and radiation imaging.

* Corresponding author at: Optical Coatings Group, Department for Energy Technologies and Renewable Sources, ENEA C.R. Casaccia, via Anguillarese 301, Rome

00123, Italy.
E-mail address: anna.sytchkova@enea.it

2. Experimental details

2.1. Sample preparation and experimental parameters

Zirconia films were deposited using an R-200 Advanced system by Picosun Oy, on 3 mm thick fused silica. The deposition for 2000 cycles was performed using Tetrakis zirconium $C_8H_{24}N_4Zr$ as precursor at 700 Pa pressure and the substrate temperature of 150 °C. The chosen deposition conditions assured a relevant carbon doping level via a slightly incomplete chemical reaction on the sample surface.

The samples were then irradiated by low-energy protons (100 keV) at fluences ranging from $1{\cdot}10^{12}$ p^+/cm^2 through $5{\cdot}10^{14}$ p^+/cm^2, Tab. 1. The irradiation was conducted at the DiFU beamline of the Laboratory for ion beam interactions, RBI. A 100 keV proton beam was obtained using the 1 MV electrostatic Tandetron accelerator with a terminal voltage of 50 kV. Prior irradiation, the chamber was evacuated down to $5{\cdot}10^{-6}$ - $5{\cdot}10^{-7}$ mbar. The beam was scanned over the sample using electrostatic scanners in order to homogenize the dose, and the current was monitored with periodic Faraday cup insertions, as well as readings from slits touching the outside of the beam. The area scanned is defined by the slits and was set to 1 x 1.5 cm^2, and 1.5 x.1.5 cm^2, depending on the sample..

Table 1
Irradiation conditions for the samples.

Sample	Fluence (p^+/cm^2)	Average rate (p^+/cm^2 s)
7	1,00E+12	1,67E+10
10	1,00E+12	1,67E+10
8	2,00E+13	1,08E+10
11	2,00E+13	1,04E+10
9	5,00E+14	1,12E+11
12	5,00E+14	2,04E+10
FS A	1,00E+12	1,71E+10
FS B	5,00E+14	6,81E+10

2.2. Characterization techniques

Optical, microstructural and compositional properties of the C-doped zirconia samples have been thoroughly investigated before and after proton irradiation [23].

For this study, the XPS data were acquired for pristine and for irradiated samples using Thermo Fisher K-Alpha spectrometer. The chemical composition of the films was studied for the film surface and in-depth profile of the main bands of Zr, O and C elements.

Photo-induced luminescence was measured by a FluoroMax 4 spectrofluorometer (Horiba Jobin Yvon, Edison, NJ, USA). Adjustment of the position of the sample was necessary in order to get an incidence angle of 30°.

3. Characterization results and discussion

3.1. XPS analysis

Carbon doping on zirconia was obtained through incomplete chemical reaction at the last stage of the film growth. For this reason, the film resulted inhomogeneous in its upper 5% of thickness, approximately. Fig. 1 reports PL maps obtained for pristine zirconia sample (a) and bare fused silica substrate (b), while Fig. I in the Supporting Information (S.I.) gives PLE spectrum. The PL and PLE data show that the visible emission around 450 nm can be activated by three possible transitions as schematically illustrated in Fig. 5 of Ref.[30]: the first one (I) at higher energies (λ_{exc}~200 nm) may be ascribed to $\sigma \rightarrow \sigma^*$ excitation, the second one (II) at λexc~270 nm corresponds to the $\pi \rightarrow \pi^*$ excitation, while the third one (III) at λexc~360 nm corresponds to the $n \rightarrow \pi^*$ excitation. For all three transitions, the emission is due to radiative decay from π^* level to n defects levels inside $\pi \rightarrow \pi^*$ gap. For the transition I the radiative decay is accompanied by non-radiative decay from σ^* to π^* level.

XPS measurements were collected for Zr3d (Fig 2a), O1s (Fig.2b) and C1s (Fig.2c) bands at different values of penetration depth (1/3 film depth corresponding to 60 nm, 2/3 film depth corresponding to 120 nm and bottom at 170 nm from the surface). For Zr3d band, high resolution XPS spectra reveal typical behavior observed for ZrO_2 film. In particular two main peaks were recorded whose values of binding energy have been reported in Fig. 2c for different penetration depth, corresponding to $Zr3d_{5/2}$ and $Zr3d_{3/2}$. As a result of the fitting procedure, it was obtained that the XPS signal is attributable in large part to the maximum coordination for zirconium (Zr^{4+}) with a presence of a specie indicated as Zr-C whose binding energy is positioned between that of metallic Zr (positioned around 279 eV) and that relative to Zr^{4+}. Hence, the broad peak marked as Zr-C is assigned to zirconium bonded to the carbon atom. The presence of the Zr-C bond is confirmed by the Zr-C bond signal revealed on C1s band reported in Fig. 2a.

The spin-orbital splitting, calculated as a function of film depth, gave values equal to 2.30 eV, 2.36 eV and 2.25 eV for 1/3 of the depth, 2/3 and bottom regions, respectively. The value closer to the theoretical one 2.39-2.40 eV reported in [31] was found for 2/3 of depth, whereas the value for the bottom of the sample is quite low and far away from the ideal value, probably due to the interaction with the substrate. However for each sample analyzed, no sub-oxides compounds as Zr_2O_3 and ZrO were detected. It means that the ZrO_2 is the predominant oxidized specie [31]. On the other hand, adsorbed oxygen as Oad can be present [31].

By comparing XPS for C1s and Zr3d bands acquired for the film surface and reported in Fig. 2d, we notice that the absence of the Zr-C band in both spectra means that the carbon on the surface is not bonded to zirconium. In Fig. 2d the XPS profile is completely resolved by fitting the curve with two Gaussian curves corresponding to $3d_{5/2}$ and $3d_{3/2}$ states. The intensity ratio of the $3d_{3/2}$ band normalized with respect to the intensity of the $3d_{5/2}$ band is around 0.71 on the surface of the film, while it increases to 0.89 for 1/3 of depth, then slightly decreases to 0.87 (2/3 depth) and finally to 0.83 at the bottom of the sample. The higher value of the intensity ratio inside the film is due to the decrease of the $3d_{5/2}$ intensity band while the Zr-C signal increases along the film depth. This behavior let us infer that, as the carbon content increases along the film depth, the number of Zr(4+)-C bonds increases too. The bonding of zirconium with carbon determines the appearance of a $3d_{5/2}$ band shifted toward lower binding energy (181 eV) with respect to the $3d_{5/2}$ band positioned around 182 eV for Zr bounded to oxygen atoms. Basically, due to the lower electronegativity of carbon with respect to oxygen, the $Zr3d_{5/2}$ binding energy is lower for zirconium atoms bonded to carbon atoms with respect to zirconium atoms bonded to oxygen.

In the O1s peak, a smaller contribution assigned to the O-H band (maybe the signal encloses also the Oad chemisorbed contribution) was included as Gaussian broadening to the best-fit procedure, Fig. 2b.

The XPS signal for the C1s band was fitted by three components corresponding to hydrocarbon bond C-H, oxygen bond C-O and Zr-C bond, Fig 2a, while only two contribution C-H and C-O were employed to fit the C1s band at the top of the film, Fig. 2d. The shift < 285 eV of the band C1s is more likely due to C-H bond and not to C-C bond, which is generally found around 285 eV.

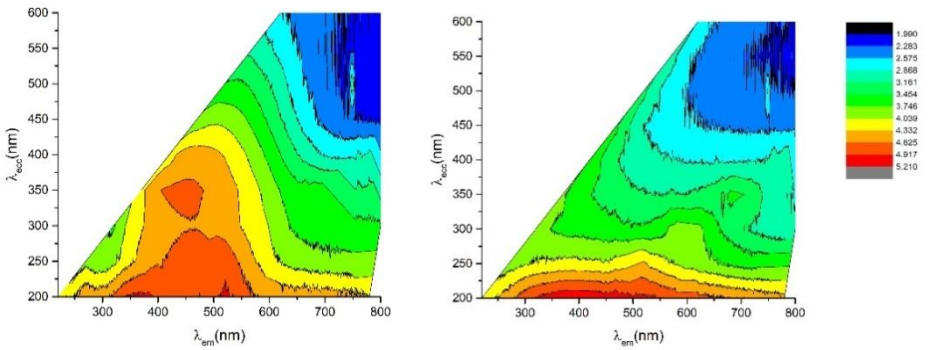

Fig. 2 PL maps for a pristine ZrO_2 film on fused silica (left) and on the naked fused silica substrate (right). The excitation wavelengths and the corresponding emission wavelengths are given on the y and x-axes, respectively.

(a)

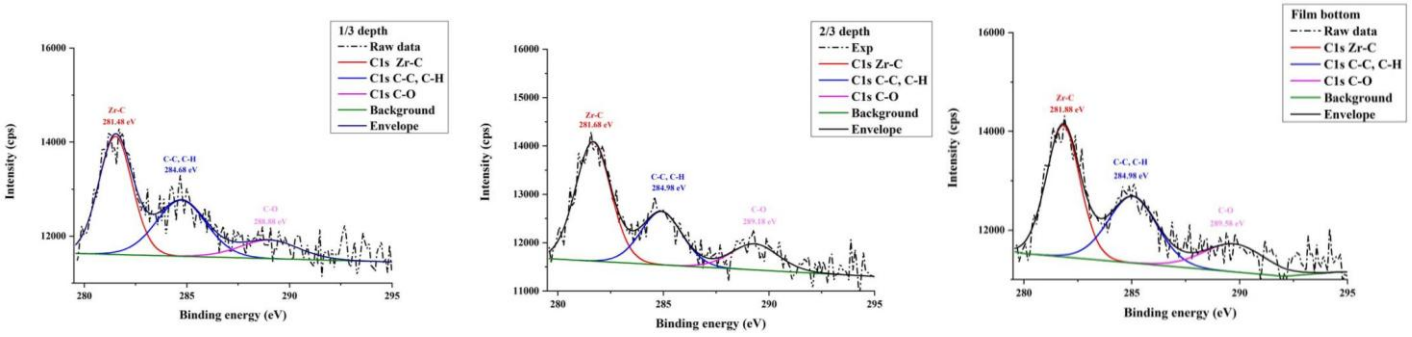

(b)

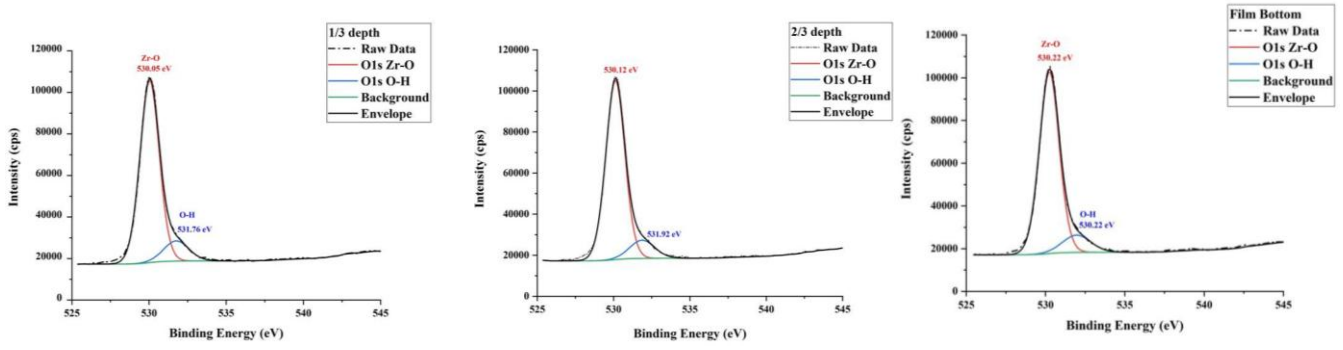

(c)

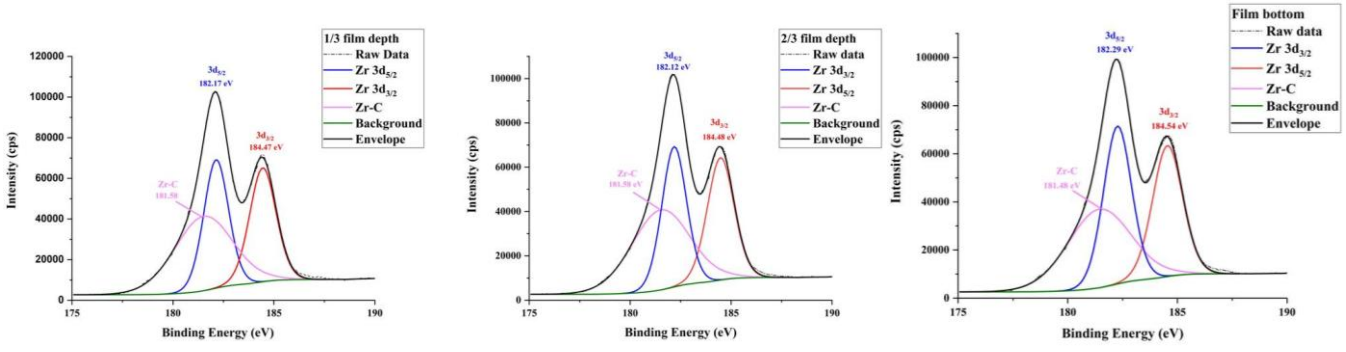

(d)

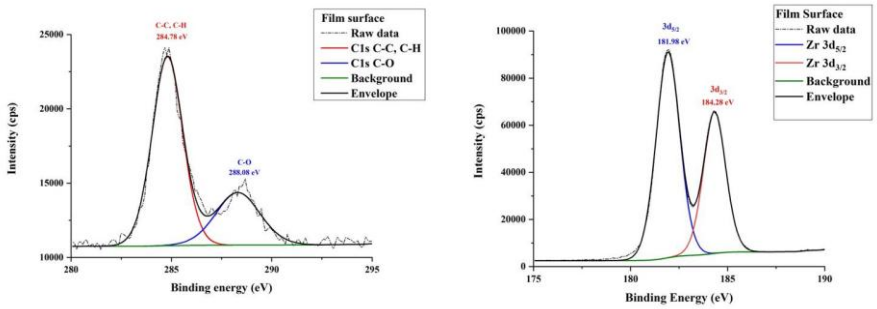

Fig. 2 Evolution of the principle XPS bands for carbon (a), oxygen (b) and zirconium (c) along the thickness of a pristine ZrO_2 films. Comparison of C1s and Zr3d bands acquired for the film surface (d).

After proton irradiation, for all the samples a general increase of the intensity (and area) ratio was observed calculated as IC-H/IC-Zr (AC-H/AC-Zr) (Table I in S.I.). In particular this effect is more evident for the samples 9A and 12A (fluence of $5 \cdot 10^{14}$ p^+/cm^2), along the entire film thickness but especially at the film bottom, whereas this ratio is slightly lower for the samples irradiated at lower dose (7A and 10A, fluence $1 \cdot 10^{12}$ p^+/cm^2). In particular, for the sample 7A and 10A, protonation induced an increase of the C-H signal with respect to Zr-C exclusively at the top layer of the film, i.e. at 1/3 of the film thickness (60 nm). Regarding the ratio $I_{Zr\text{-}C}/I_{Zr3d5/2}$ ($A_{Zr\text{-}C}/A_{Zr3d5/2}$) (Table 2 in S.I), we observe that it suffers a general decrease for the irradiated sample with respect to the pristine one, regardless of the depth, indicating that Zr-C bonds decrease with respect to Zr-O bonds along all the thickness of the film. Moreover, considering the ratio $I_{O\text{-}H}/I_{O\text{-}Zr}$ ($A_{O\text{-}H}/A_{O\text{-}Zr}$) (Table III in S.I) we infer that O-H bonds slightly increase with respect to Zr-O bonds for the irradiated samples, along all the film thickness, especially for the two samples irradiated at highest doses. Therefore we can conclude that protonation induces the cleavage of Zr-C bonds in favor of C=O and C-H formation, deeper in the sample as the dose increases, and it favors the formation of O-H bonds.

3.2. *Analysis of PL maps*

Fig.3 reports PL maps for irradiated samples together with the element abundancy retrieved from the survey spectrum taken at the surface of the irradiated samples. The atomic percentage as a function of the etching time is given for all the irradiated samples in Fig. III of S.I (with 1200 s of etching time corresponding to a penetration depth of 120 nm). As one can note in Fig. 3, the PL intensity ratio of Transition III with respect to Transition I and II increases for the two samples irradiated at higher doses, maybe due to the higher content of carbon partially bonded to oxygen which form n-levels inside π-π^* gap. In fact, oxygen content on the surface is very high, giving a ratio with Zr content much higher than the value expected for stoichiometric zirconia (O/Zr=2), especially for samples protonated at higher doses for whom the O/Zr ratio gets values up to 7 and 12. In particular, the ratio between C=O and C-Zr bonds is higher for the irradiated samples as compared to the pristine samples (see Table I in S.I), and it increases with the dose. C=O bonds in carbon materials are known to be responsible for the emission at λ_{em}=450 nm excited at λ_{exc}=300 nm (Transition III) [30]. Therefore, this kind of emission is more intense for high dose-irradiated samples most probably due to the higher abundance of C=O bonds. The carbon increases on the surface along the radiation dose is due to the build-up of a carbonaceous contamination layer during the irradiation [23]. Although very thin (determined as 0.7 nm for the highest of used fluences [23]) such a layer is sufficiently thick to influence the survey mean values as the probing beam of the XPS penetrates under the surface for approximately 5 nm which is comparable with the thickness of the contamination layer rich in carbon.

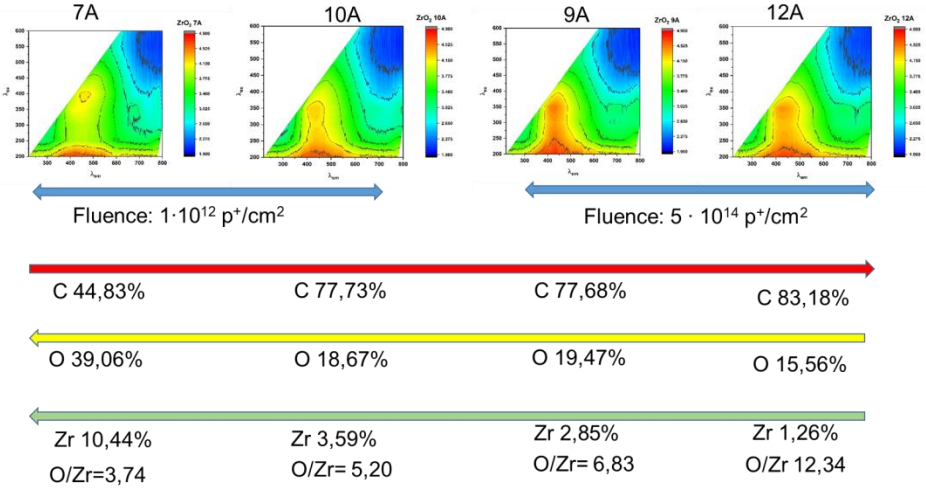

Fig. 3 PL maps for a irradiated ZrO_2 films. Modification of the content of carbon, oxygen and zirconium on the films surface due to irradiation.

It is worth mentioning that during the proton irradiation, plasma creation was observed, Fig. 4. A movie with registered discharges is available as a supplementary material. Upon proton irradiation the films underwent compositional modification

Fig. 4 A pho a substrate.

Typical charging the dielectric substrate induced by the charged particles can provoke discharge phenomena with partial combustion reaction in the film that can be expressed as Eq. (1)

( ) ( )

(1)

Protonation reaction expressed by Eq. (2) was also possible under the proton irradiation followed by prompt combustion of the formed methane thanks to oxygen excess in the over-stoichiometric pristine film.

( ) ( )

(2)

Reactions (1) and (2) can justify the lower abundance of C-H bonds on the surface of samples irradiated with higher doses and also the decrease under irradiation of Zr-C bonds with respect to Zr-O bonds, expressed by the ratio $I_{Zr\text{-}C}/I_{Zr3d5/2}$ ($A_{Zr\text{-}C}/A_{Zr3d5/2}$) reported in Table I in the S.I..

Summarizing, the XPS depth-resolved investigations revealed the establishment of O-H and C-H bonds deeper in the film as the dose increases. Due to reactions mechanisms (1) and (2) the C-H bonds on the surface most probably decrease due to methane or water vapor release under irradiation and this mechanism is more evident for high dose irradiation. For the same reason, the ratio of Zr-C over Zr-O bonds decreases in the film under irradiation (see XPS Zr3d signal analysis in S.I.). Concerning the remaining carbon content, the percentage of carbon bonded to oxygen becomes higher for the samples irradiated at higher dose and this effect induces the increase of PL emission at λ_{em}= 450 nm excited at λ_{exc}=300 nm (Transition II) with respect to the emission at λ_{em}=450 nm excited at λ_{exc}=200-270 nm (Transition I).

Fig. 5 gives a comparison between PL maps of each sample before and after irradiation and it is evident that the decrease of emission intensity for all the analyzed irradiated samples. This is due to reduction of carbon-zirconium bonds and decrease of carbon content inside the film upon the irradiation following the reactions (1) and (2).

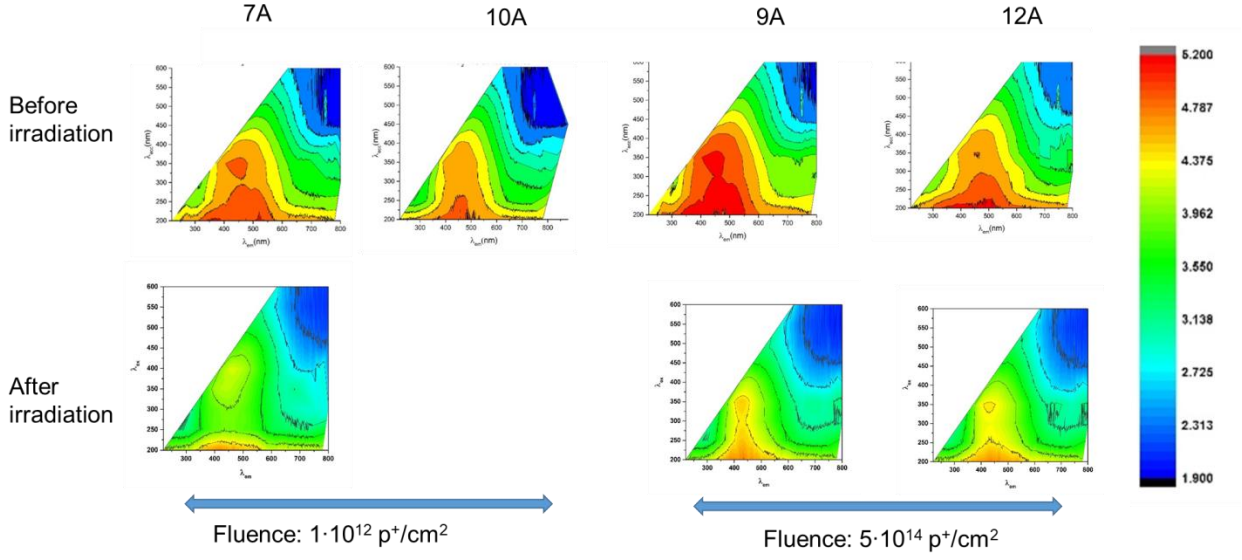

Fig. 5 PL maps for pristine (upper frame) and irradiated (lower frame) ZrO2 films. Modification of the content of carbon, oxygen and zirconium in the films due to irradiation

3.3. *Theoretical simulation of proton-induced damage in C-doped ZrO_2*

In simulating the structural effects of proton irradiation in amorphous C-doped zirconia, the "Detailed calculation with full damage cascades" mode in SRIM [32] was employed, and the parameters listed in Tab. 2 were adopted.

Tab. 2 Parameters adopted in the SRIM simulation of 100 keV proton irradiation in C-doped ZrO_2

Atom	Zr	O	C
Stoichiometry	1	2	0.001
Displacement energy (eV)	25	28	28
Lattice Binding Energy (eV)	3	3	3
Surface Binding Energy (eV)	6.33	2	7.41
Mass density (g cm^{-3})		5.68	

It is worth remarking that the reported carbon concentration is defined on a "upper limit" basis, and even in this case the effect of carbon incorporation in the ZrO_2 matrix can be regarded as negligible in terms of the modeled depth profile of the linear density of induced vacancies. From such profile (reported in Fig. 6) it is possible to estimate the geometrical features summarized in Tab. 3.

Tab. 3 Geometrical ion penetration features for 100 keV protons in carbon-doped zirconia

Direction	Range (nm)	Straggle (nm)
Longitudinal	542	85
Lateral projection	88	112
Radial	138	78

The damage density linearly increases from the film surface towards its depth. This means that the inner part of the film undergoes heavier impact from the radiation. The film material undergoes the structural transformations analyzed in the previous section. The occurrence of these effects is larger in the upper part of the film due to higher concentration of the impurities. On the other hand, the proton impact increases along the film depth. These two effects induce film densification and lead to a more uniform film. After irradiation, the upper layer rich in impurities result much thinner, which the rest of the film result less absorbing [24].

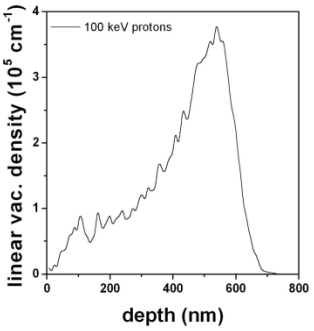

Fig. 6 Linear vacancy density profile induced by 100 keV protons in carbon-doped zirconia

4. Conclusions

Amorphous C-doped zirconia thin films obtained using ALD technique on fused silica substrates have high transmittance and significant PL capacity. Carbon doping on zirconia was obtained through incomplete chemical reaction at the last stage of the film growth. Due to the carbon doping, zirconia films present three main PL transitions: Transition I and II at λ_{em}=450 nm (λ_{exc}=200 and 270 nm), related to sp3 and sp2 C-C bonds, and Transition II at λ_{em}=450 nm (λ_{exc}=300 nm) that can be assigned to C=O bonds which introduce n levels in the π- π* gap.

Since the high transparency of the films in the visible range is preserved by limiting the carbon content, the carbon-doped zirconia may find application as transparent material to convert high energy into lower energy photons. Moreover, thanks to the substantial change of its optical properties under irradiation, the C-doped zirconia may find application as optical sensor of radiation. In this study we hence investigated how the PL properties in C-doped zirconia films on silica substrate change under proton radiation.

The films underwent low-energy proton irradiation with energy of 100 keV and two values of proton fluences ($1{\cdot}10^{12}$ p^+/cm^2 and $5{\cdot}10^{14}$ $p^+/cm2$) were used. The changes induced by the radiation on the chemical composition of the films have been monitored as a function of irradiation dose. To this aim, the in-depth resolved XPS analyses have been performed on both the pristine and irradiated samples. The ratio Zr-C/Zr-O bonds decreases under irradiation while the ratio C-H/C-Zr bonds increases, especially at higher doses. Analogously, the ratio C=O/C-Zr bonds increases with respect to pristine samples, especially for high-dose irradiated samples. Therefore, we can conclude that C-Zr bonds are cleaved by protonation in favor of Zr-O, C-H and C=O bonds establishment. As a consequence, more defects levels are formed in the π-π* gap of carbon. Consequently, the emission due to Transitions I becomes more intense for high energy doses, getting intensity values close to Transitions I/II.

Declaration of Competing Interest

The authors declare that they have no known competing financial interests or personal relationships that could have appeared to influence the work reported in this paper.

Data availability

Data may be obtained from the authors upon reasonable request.

Acknowledgments

This work was performed with contribution of the Italian Ministry for University and Research and the Italian Ministry of Foreign Affairs, PGR AstroOptElect "Effects of space environment on optical and electronic devices for astrophysical space missions". China-Italy Intergovernmental Cooperation Project under the National Key R&D program of China (2018YFE0118000).

The authors are thankful to Martino Palmisano and Emanuela Pesce from ENEA Brindisi Lab for their outstanding technical support in sample characterization.

References

1. Z. Chen, Q. Xu, K. Zhang, W.-H. Wong, D.-L. Zhang, E. Y.-B. Pun and C. Wang, Efficient erbium-doped thin-film lithium niobate waveguide amplifiers, Opt. Lett. 46 (2021) 1161 DOI: 10.1364/OL.420250

2. G. Adamopoulos, S. Thomas , P. Wöbkenberg, D. Bradley, M. McLachlan and T. Anthopoulos, "High-Mobility Low-Voltage ZnO and Li-Doped ZnO Transistors Based on ZrO2 High-k Dielectric Grown by Spray Pyrolysis in Ambient Air", Adv. Mater., 2011, 23 , 1894-1898.

3. D. Clarke and S. Phillpot , "Thermal barrier coating materials", Mater. Today, 8 (2005), 22-29.

4. Hojabri, A. Structural and optical characterization of ZrO2 thin films grown on silicon and quartz substrates. J Theor Appl Phys 10, 219–224 (2016). https://doi.org/10.1007/s40094-016-0218-8

5. M. Jerman, Z. Qiao, and D. Mergel, "Refractive index of thin films of SiO2, ZrO2, and HfO2 as a function of the films' mass density," Appl. Opt. 44, 3006-3012 (2005). https://doi.org/10.1364/AO.44.003006

6. S. Heiroth, R. Ghisleni, T. Lippert, J. Michler, A. Wokaun Optical and mechanical properties of amorphous and crystalline yttria-stabilized zirconia thin films prepared by pulsed laser deposition, Acta Materialia 59 (2011) 2330, https://doi.org/10.1016/j.actamat.2010.12.029

7. Lakshmi, J.S., John Berlin, I., Daniel, G.P., Thomas, P.V., Joy, K., Effect of calcination atmosphere on photoluminescence properties of nanocrystalline ZrO2 thin films prepared by solgel dip coating method, Physica B: Condensed Matter, 406 (2011), 3050. https://doi.org/10.1016/j.physb.2011.05.004

8. M.A. Botzakaki, N. Xanthopoulos, E. Makarona, C. Tsamis, S. Kennou, S. Ladas, S.N. Georga, C.A. Krontiras, ALD deposited ZrO2 ultrathin layers on Si and Ge substrates: A multiple technique characterization, Microelectronic Engineering 112 (2013), 208-212. https://doi.org/10.1016/j.mee.2013.03.002.

9. L. Song, X. Cao, L. Li, "Engineering Stable Surface Oxygen Vacancies on ZrO2 by Hydrogen-Etching Technology: An Efficient Support of Gold Catalysts for Water-Gas Shift Reaction", ACS Applied Materials and Interfaces 10(2018), 31249-31259

10. S.J. Malode, N.P. Shetti, "ZrO2 in biomedical applications" in Metal Oxides for Biomedical and Biosensor Applications , 2021, p.471-501 DOI: 10.1016/B978-0-12-823033-6.00016-8

11. T. Liu, X. Zhang, X. Wang, et al. "A review of zirconia-based solid electrolytes". Ionics 22 (2016), 2249–2262 https://doi.org/10.1007/s11581-016-1880-1

12. Kalita, P., Ghosh, S., Gutierrez, G. et al. Grain size effect on the radiation damage tolerance of cubic zirconia against simultaneous low and high energy heavy ions: Nano triumphs bulk. Sci Rep 11, 10886 (2021). https://doi.org/10.1038/s41598-021-90214-6

13. K.E. Sickafus, Hj. Matzke, Th. Hartmann, K. Yasuda, J.A. Valdez, P. Chodak, M. Nastasi, R.A. Verrall, "Radiation damage effects in zirconia", Journal of Nuclear Materials, 274 (1999), 66-77, DOI: 10.1016/S0022-3115(99)00041-0

14. V. Ponnilavan, M. Mushtaq Alam, M. Ezhilan, Kalpana Pandian, S. Kannan, "Structural, mechanical, morphological and optical imaging characteristics of Yb3+ substituted zirconia toughened alumina," Materials Today Communications, 24 (2020) 100983, DOI:10.1016/j.mtcomm.2020.100983.

15. K. Smits, L. Grigorjeva, D. Millers, A. Sarakovskis, J. Grabis, W. Lojkowski, Intrinsic defect related luminescence in ZrO2, J. Lumin., 131 (2011) 2058-2062, DOI: 10.1016/j.jlumin.2011.05.018.

16. A. King, R. Singh, R. Anand, S.K. Behera, B.B. Nayak, Phase and luminescence behaviour of Ce-doped zirconia nanopowders for latent fingerprint visualisation, Optik 242 (2021),167087. https://doi.org/10.1016/j.ijleo.2021.167087.

17. Hui, Y., Zou, B., Liu, S., Zhao, S., Xu, J., Zhao, Y., Fan, X., (...), Cao, X., Effects of Eu3+-doping and annealing on structure and fluorescence of zirconia phosphors, Ceramics International, Part PB 41 (2015), 2760-2769. https://doi.org/10.1016/j.ceramint.2014.10.091

18. Kobayashi, K., Kuwajima, H., Masaki, T., Phase change and mechanical properties of ZrO2-Y2O3 solid electrolyte after ageing, Solid State Ionics, 3-4 (1981), 489. doi: 10.1016/0167-2738(81)90138-7

19. R. Di Monte, Kašpar, J., Nanostructured CeO2-ZrO2 mixed oxides, J. Materials Chemistry, 15 (2005), 633. https://doi.org/10.1039/b414244f

20. D.H.A. Besisa, E.M.M. Ewais, Black zirconia composites with enhanced thermal, optical and mechanical performance for solar energy applications, Solar Energy Materials and Solar Cells, 225 (2021), 111063, doi:

10.1016/j.solmat.2021.111063.

21. E. Aleksanyan, M. Kirm, E. Feldbach, K. Kukli, S. Lange, I. Sildos, A. Tamm, Luminescence properties of Er3+ doped zirconia thin films and ZrO2/Er2O3 nanolaminates grown by atomic layer deposition, Optical Materials, 74 (2017), 27-33, DOI: 10.1016/j.optmat.2017.05.003

22. S.V. Nikiforov, A.A. Menshenina, S.F. Konev, The influence of intrinsic and impurity defectsnon the luminescence properties of zirconia, J. Lumin. 212 (2019), 219 https://doi.org/10.1016/j.jlumin.2019.03.062

23. A. Sytchkova, M.L. Protopapa, P. Olivero, L. Tapfer, E. Burresi, T. Dunatov, Z. Siketic, M. Palmisano, E. Pesce, Y. Wang, Z. Wang, H. He, Optical characterization of the impact of 100 keV protons on the optical properties of ZrO2 films prepared by ALD on fused silica substrates, submitted to Appl.Opt.

24. K. Smits, L. Grigorjeva, D. Millers, A. Sarakovskis, J. Grabis, W. Lojkowski, Intrinsic defect related luminescence in ZrO2, J. Lumin. 131 (2011), 2058. https://doi.org/10.1016/j.jlumin.2011.05.018

25. S.V. Nikiforov, A.A. Menshenina, S.F. Konev, The influence of intrinsic and impurity defectsnon the luminescence properties of zirconia, J. Lumin. 212 (2019), 219 https://doi.org/10.1016/j.jlumin.2019.03.062

26. T. Wang, G. Wang, M. Qiu, W. Cheng, J. Zhang, G. Zhao, The origin of the 500 nm luminescence band related to oxygen vacancies in ZrO2, J. Lumin. 237 (2021), 118133, https://doi.org/10.1016/j.jlumin.2021.118133.

27. M. Rushton, I. Ipatova, L. Evitts, W. Lee, S. Middleburgh, Stoichiometry deviation in amorphous zirconium dioxide, RSC Adv., 2019, 9, 16320-16327 https://doi.org/10.1039/C9RA01865D

28. D. Islamov, V. Gritsenko, T. Perevalov, V. Aliev, V. Nadolinny, A. Chin, Oxygen Vacancies in Zirconium Oxide as the Blue Luminescence Centres And Traps Responsible for Charge Transport: Part II - Films. 2020. http://dx.doi.org/10.2139/ssrn.3708728

29. M. Owen, M. Rushton , L. Evitts , A. Claisse, M. Puide, W. Lee, S. Middleburgh, Diffusion in doped and undoped amorphous zirconia, J. Nuclear Materials (2021) 153108. https://doi.org/10.1016/j.jnucmat.2021.153108

30. ML, Protopapa, E. Burresi, M. Plamisano, E. Pesce, L. Latterini, N. Taurisano, G. Quaglia, R. Mazzaro, V. Morandi, Changing the Microstructural and Chemical Properties of Graphene Oxide Through a Chemical Route, Appl Spectrosc. 76 (2022) 1452-1464. doi: 10.1177/00037028221127048

31 C. Morant, J.M. Sanz, L. Galan, L. Solriano, F, Rueda, " An XPS study of the interaction of oxygen with zirconium", Scurface Science, 218 (1989) 331-345. Doi:10.1016/0039-6028(89)90156-8

32 J. F. Ziegler, J. P. Biersack, M. D. Ziegler, "SRIM – The Stopping and Range of Ions in Matter", Mormsville, NC: Ion Implantation Press (2008)

Supporting Information

Tab.I Parameters of Gaussian curves obtained from deconvolution of C band

Sample	Depth	C-Zr			C-H, C-C			C=O		
		BE (eV)	Height Ratio	Area Ratio	BE (eV)	Height Ratio	Area Ratio	BE (eV)	Height Ratio	Area Ratio
Pristine	60 nm	281.48	1	1	284.68	0.47	0.73	288.88	0.15	0.28
	120 nm	281.68	1	1	284.98	0.46	0.57	289.18	0.22	0.32
	170 nm	281.88	1	1	284.98	0.51	0.74	289.58	0.21	0.39
9-A Fluence $5{\cdot}10^{14}$	60 nm	281.72	1	1	284.76	0.60	0.70	288.90	0.25	0.44
	120 nm	281.60	1	1	284.62	0.61	1.19	289.84	0.27	0.58
	170 nm	281.57	1	1	284.73	0.72	0.88	289.63	0.21	0.41
12-A Fluence $5{\cdot}10^{14}$	60 nm	281.72	1	1	284.78	0.51	0.82	290.03	0.23	0.44
	120 nm	281.63	1	1	284.60	0.54	0.85	289.65	0.18	0.34
	170 nm	281.66	1	1	284.71	0.57	0.74	289.07	0.20	0.37
7-A Fluence $5{\cdot}10^{14}$	60 nm	281.53	1	1	284.65	0.57	0.69	289.02	0.18	0.34
	120 nm	281.47	1	1	284.62	0.44	0.65	289.26	0.21	0.10
	170 nm	281.50	1	1	284.68	0.49	0.80	289.47	0.18	0.36
10-A Fluence $5{\cdot}10^{14}$	60 nm	281.67	1	1	284.59	0.61	0.68	289.14	0.20	0.36
	120 nm	281.64	1	1	284.67	0.62	0.83	288.46	0.24	0.43
	-	-	-	-	-	-	-	-	-	-

Tab. II Parameters of Gaussian curves obtained from deconvolution of Zr band

Sample	Depth	Zr-3d5/2			Zr-3d3/2			Zr-C		
		BE (eV)	Height Ratio	Area Ratio	BE (eV)	Height Ratio	Area Ratio	BE (eV)	Height Ratio	Area Ratio
Pristine	60 nm	182.17	1	1	184.47	0.89	0.95	181.58	0.58	1.35
	120 nm	182.12	1	1	184.48	0.87	0.94	181.58	0.57	1.33
	170 nm	182.29	1	1	184.54	0.83	0.88	181.48	0.50	1.11
9-A Fluence $5{\cdot}10^{14}$	60 nm	182.13	1	1	184.44	0.67	0.61	180.43	0.21	0.29
	120 nm	182.12	1	1	184.44	0.68	0.62	180.45	0.20	0.28
	170 nm	182.11	1	1	184.43	0.67	0.61	180.41	0.19	0.27
12-A Fluence $5{\cdot}10^{14}$	60 nm	182.27	1	1	184.58	0.65	0.59	180.44	0.22	0.30
	120 nm	182.25	1	1	184.58	0.66	0.60	180.43	0.21	0.29
	170 nm	182.26	1	1	184.58	0.66	0.59	180.44	0.21	0.29
7-A Fluence $1{\cdot}10^{12}$	60 nm	181.52	1	1	183.85	0.65	0.58	179.62	0.21	0.29
	120 nm	181.54	1	1	183.88	0.65	0.57	179.62	0.21	0.28
	170 nm	181.56	1	1	183.89	0.65	0.57	179.66	0.21	0.28
10-A Fluence $1{\cdot}10^{12}$	60 nm	182.17	1	1	184.50	0.66	0.60	180.35	0.21	0.29
	120 nm	182.17	1	1	184.50	0.65	0.58	180.33	0.21	0.28
	-	-	-	-	-	-	-	-	-	-

Tab.III Parameters of Gaussian curves obtained from deconvolution of O band.

Sample	Depth	Zr-O			O-H		
		BE (eV)	Height Ratio	Area Ratio	BE (eV)	Height Ratio	Area Ratio
Pristine	60 nm	530.08	1	1	531.78	0.12	0.16
	120 nm	530.08	1	1	531.88	0.10	0.15
	170 nm	530.28	1	1	531.98	0.10	0.15
9-A Fluence $5{\cdot}10^{14}$	60 nm	529.97	1	1	531.56	0.13	0.19
	120 nm	529.93	1	1	531.42	0.14	0.23
	170 nm	529.93	1	1	531.69	0.12	0.16
12-A Fluence $5{\cdot}10^{14}$	60 nm	530.05	1	1	531.68	0.12	0.18
	120 nm	530.04	1	1	531.73	0.11	0.15
	170 nm	530.05	1	1	531.77	0.12	0.16
7-A Fluence $1{\cdot}10^{12}$	60 nm	529.95	1	1	531.64	0.12	0.15
	120 nm	529.96	1	1	531.70	0.11	0.14
	170 nm	529.96	1	1	531.66	0.11	0.14
10-A Fluence $1{\cdot}10^{12}$	60 nm	530.00	1	1	531.75	0.11	0.14
	120 nm	529.98	1	1	531.75	0.11	0.14
	-	-	-	-	-	-	-

Fig. I. PLE curves giving emission at λ_{em}=442 nm maps for pristine samples

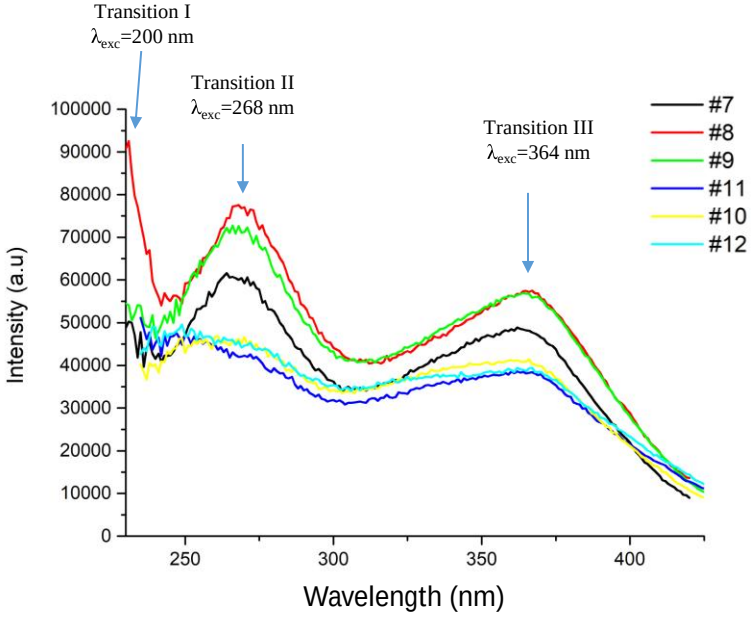

Fig. II. Atomic percentage as a function of etching time for the irradiated sample

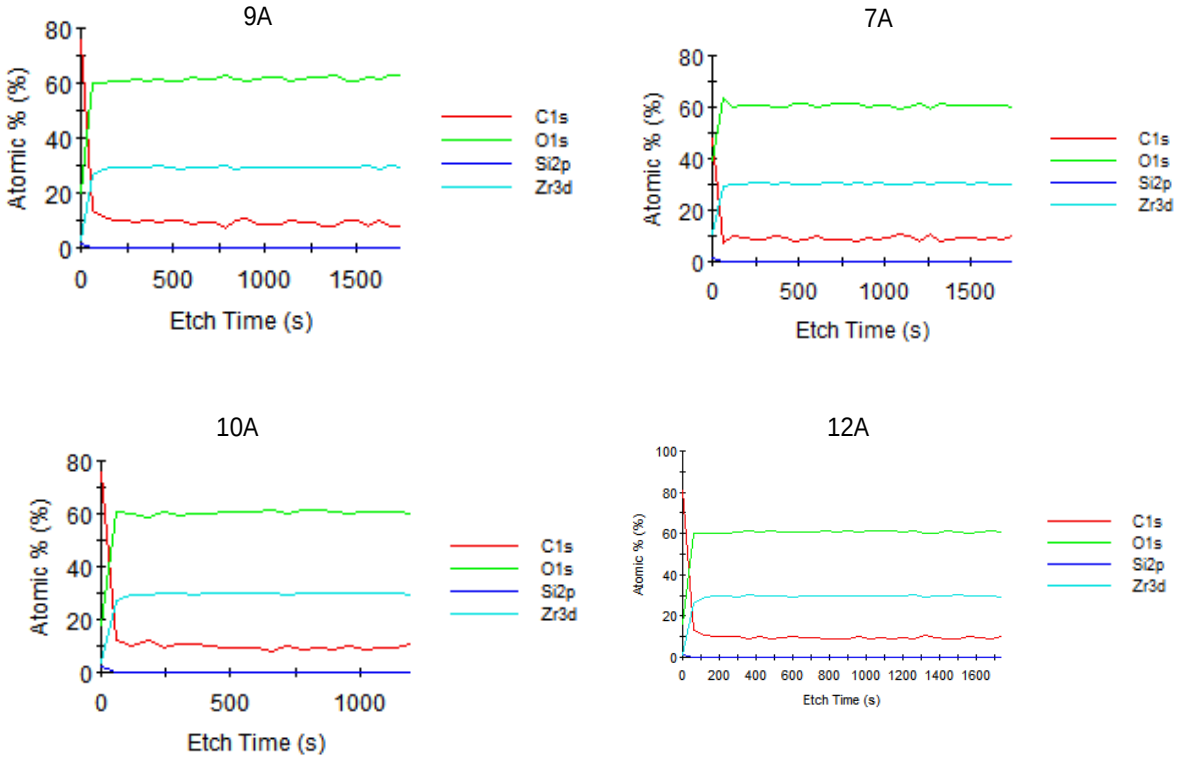

Graphical abstract